Available online at www.sciencedirect.com
ScienceDirect
Trans. Nonferrous Met. Soc. China 35(2025) 2183−2200
Transactions of Nonferrous Metals Society of China
www.tnmsc.cn

Microstructure and high-temperature performance of heat-resistant Al−Fe−Mn alloy prepared by laser powder bed fusion

Jun-sheng CHEN[1], Ji-bing CHEN[1], Qian-yu SHI[1], Yue-ting WANG[2], Xi-zhen XIA[2], Rui-di LI[2]

1. School of Mechanical Engineering, Wuhan Polytechnic University, Wuhan 420023, China;
2. State Key Laboratory of Powder Metallurgy, Central South University, Changsha 410083, China

Received 6 June 2024; accepted 19 November 2024

Abstract: With the laser remelting of cast alloys combined with non-equilibrium liquidus projection thermodynamic calculations, a high-strength and heat-resistant Al−3Fe−2Mn alloy was designed. Incorporating Mn atoms into the metastable nanoscale Al_6Fe phase, occupying some lattice sites, enhances its thermal stability. Additionally, during rapid solidification of laser powder bed fusion (L-PBF), the solubility of Fe and Mn elements in the aluminum alloy increases significantly, forming a supersaturated solid solution with improved strength. This alloy demonstrates excellent processability, achieving a relative density of over 99%, and tensile strengths of 295 MPa at 200 °C and 230 MPa at 300 °C. The Al−3Fe−2Mn alloy holds great potential for wide applications due to its high strength at high temperature.

Key words: Al−Fe−Mn alloy; laser powder bed fusion; high-temperature strength; microstructure; heat-resistant property

1 Introduction

Aluminum alloys play a crucial role in aerospace and rail transport industries due to their outstanding strength, easy processing, and superior corrosion resistance. These qualities are highly sought in applications emphasizing lightweight structures and efficiency [1−3]. Given the critical role of aluminum alloys at high temperature for aerospace component's design, they must satisfy stringent aerodynamic and lightweight construction criteria [4]. Laser powder bed fusion (L-PBF), an advanced technique in metal's additive manufacturing (AM) [5−8], is suitable for manufacturing various aluminum alloys [9,10]. It facilitates the creation of complex structures while enhancing the material's mechanical performance through a rapid solidification process [11]. This process encourages the formation of supersaturated solid solutions and fine precipitates, obtaining improved overall performance of material [12,13].

Recent research has explored the production of heat-resistant aluminum alloys enhanced with transition metals such as copper (Cu), nickel (Ni), zirconium (Zr), and chromium (Cr) using L-PBF [14−20]. Notably, DENG et al [15] developed an Al−5.7Ni alloy that exhibited crack-free characteristic and high strength, achieved through optimized printing parameters. At ambient temperature, this alloy demonstrated a tensile strength of 410 MPa, which is maintained at 140 MPa even at a high temperature of 300 °C. The high performance should be attributed to the dispersion strengthening from Al_3Ni nanoparticles. Conversely, SHYAM et al [21] reported on an Al−Cu−Mn−Zr alloy processed by AM L-PBF, which shows promising mechanical performance at room temperature with a tensile strength exceeding 400 MPa, enhanced by the addition of trace rare

Corresponding author: Ji-bing CHEN, Tel: +86-27-85617871, E-mail: jbchen@whpu.edu.cn
https://doi.org/10.1016/S1003-6326(25)66808-7

earth elements. However, its strength significantly declines above 300 °C due to Al_2Cu phase coarsening.

Al−Fe alloys, recognized for their recyclability in engineering applications, enhance the ductility and heat resistance of aluminum alloys while diminishing their brittleness. This is achieved by optimizing the microstructure of intermetallic compounds, including refining $Al_{13}Fe_4$ (θ-Al_3Fe) phase and forming metastable Al_6Fe nanoparticles. In the work by WANG et al [22], comprehensive investigations into the microstructural evolution, crystallographic characteristics, and mechanical performance of an Al−5Fe−1Mg−0.8Sc−0.7Zr alloy prepared via L-PBF were conducted. The findings suggest that iron (Fe) contributes to the enhanced performance of the alloy through solid-solution strengthening and precipitation hardening. The presence of Al_6Fe phase at grain boundaries may facilitate grain boundary's strengthening. However, excessive Fe in aluminum alloys will adversely affect the processability of L-PBF. WANG et al [23] demonstrated this by fabricating an Al−5Fe alloy via L-PBF, where coarse θ-$Al_{13}Fe_4$ phases were observed along the melt pool boundaries. The presence of this θ phase resulted in increased brittleness, leading to the formation of pronounced cracks in the printed structure [24]. Furthermore, manganese (Mn) stabilizes the Al_6Fe phase within the α(Al) matrix, effectively inhibiting the formation of the θ phase and the phase transition from metastable Al_6Fe to the stable θ phase, thus mitigating intermetallic phase coarsening during thermal exposure.

This study employed an innovative approach to design and investigate a heat-resistant aluminum alloy. By utilizing a systematic rescanning approach, we precisely elucidate the role of Fe concentration in optimizing the alloy's design. The study leverages thermodynamically-driven CALPHAD simulations to guide the compositional refinement of the Al−Fe−Mn ternary alloy [25], underscoring the critical balance between composition and processing parameters. By finely tuning the key parameters in L-PBF, including laser power and scanning rate, the optimized densification of the alloy is achieved, enabling superior processability. This work offers a comprehensive framework that bridges alloy's design, microstructural evolution, and mechanical performance, paving the way for next-generation aluminum-iron alloys that excel at high temperature while maintaining the precision required for advanced AM techniques.

2 Experimental

2.1 Design of Al−Fe−Mn ternary alloys

In the Al−Fe alloy system, an increase in iron content is typically associated with enhanced heat resistance of the alloy. This correlation is attributed to the formation of metastable phases by iron within the aluminum matrix, which aids in maintaining structural stability and mechanical strength at high temperature [26]. However, in the rapid solidification environment of L-PBF, the effects of increased iron content on the microstructure and material's performance are complex and nuanced [27−29]. The optimum iron content was determined by laser scanning of the aluminum alloy ingot (Fig. 1(a)) using the same parameters. As illustrated in Fig. 1(b), for alloys ranging from Al−1Fe to Al−3Fe, a gradual increase in iron content does not significantly alter the morphology of the melt pool.

Conversely, in Al−4Fe and Al−5Fe alloys, the presence of pores and cracks within the melt pool is observed. This phenomenon may be caused by the uneven dissolution of excessive iron in the aluminum matrix, leading to uneven thermal distribution and thus, reducing the stability of the melt pool. This uneven thermal distribution is detrimental to maintaining the alloy's structural integrity at high temperature. Thus, optimizing the iron content will obtain enhanced heat resistance and mechanical performance of material at high temperature. For the Al−3Fe alloy, a small number of fine iron-rich phases are observable within the melt pool. Moreover, in the backscattered electron (BSE) mode, numerous small iron-rich phase particles are carried from the casting matrix as the laser melts the matrix due to the formation of the 'Marangoni' flow (Figs. 1(c, d)). These observations indicate that the fine particles in the Al−3Fe melt pool (Fig. 1(b)) are not solely the result of excessive iron failing to dissolve completely during the L-PBF process. Moreover, when the iron content exceeds 3%, the morphology of the melt pool in Al−4Fe and Al−5Fe alloys becomes turbid, indicating excessive precipitation of iron-rich phases rather than existing in a solid

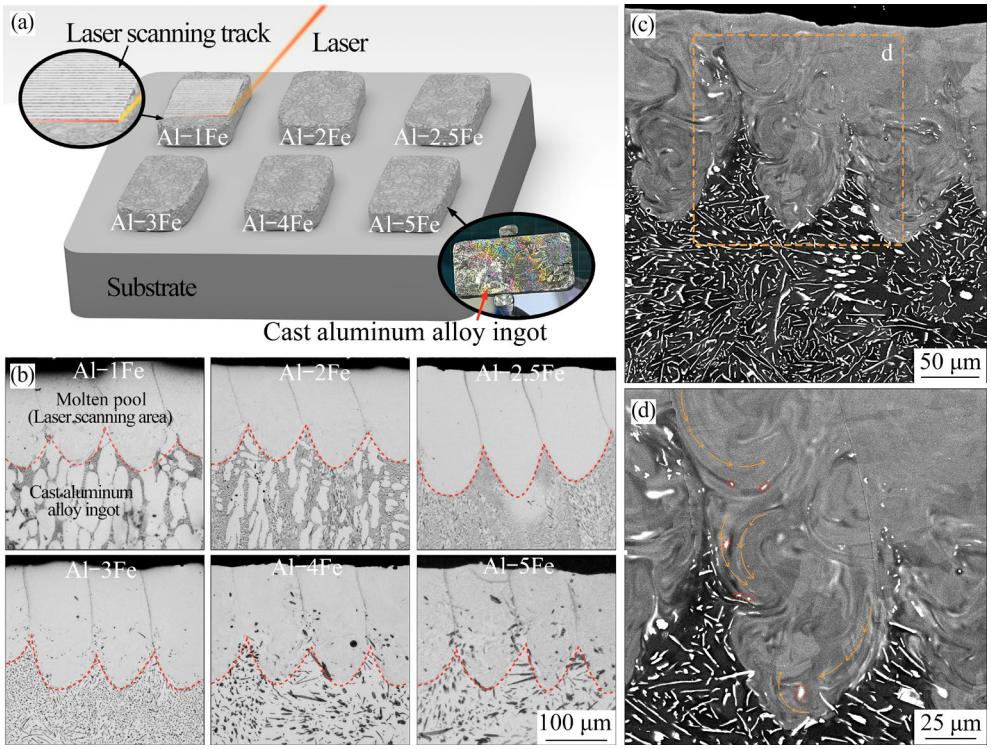

Fig. 1 Schematic diagram of laser scanning cast aluminum alloy ingot (a), morphology of molten pool of Al−*x*Fe melting matrix scanned by L-PBF at same laser power and scanning rate (b); scanning electron microscope (SEM) images of molten pool of laser scanning Al−3Fe matrix (c, d)

solution state. These precipitated phases can enhance the material's heat resistance at high temperature, but may serve as nucleation sites for cracks and other defects during the L-PBF process, thereby compromising the uniformity of the melt pool and introducing internal stresses during solidification. These stresses could reduce the material's performance. The Al−3Fe alloy achieves an optimal balance between melt pool morphology and heat resistance, exhibiting higher melt pool stability and fewer processing defects. Therefore, it is speculated that it also has high structural stability and mechanical strength in high-temperature applications. Exceeding this iron content threshold may negatively impact the microstructure and high-temperature performance during the L-PBF processing. Based on the above study, Al−3Fe can be considered as an ideal alloy composition for achieving high heat resistance and excellent manufacturability.

In addition, by taking into account of the refined $Al_6Fe/\alpha(Al)$ eutectic structure observed in fully dense L-PBF Al−Fe alloys [30], it stands to reason that alloy compositions nearing the $Al_6M/\alpha(Al)$ eutectic point are advantageous for the fabrication of fully dense Al-Fe-Mn ternary samples. The utilization of eutectic solidification aligns with the strategic design of aluminum alloys characterized by high printability [31], aimed at mitigating hot cracking during solidification [32]. To determine the optimal Mn content, the phase formation Scheil solidification diagrams for the Al−3Fe−*x*Mn alloy (x=1, 2, 3 and 4) were calculated under non-equilibrium solidification conditions, with the results depicted in Fig. 2(b). In alloys with an Mn content exceeding 2%, the primary phase is the Al_6M. Due to the adverse effects of a high volume fraction of primary Al−Fe intermetallic phases on sample densification [23], the final experimental composition of the L-PBF alloy powder was set to be Al−3Fe−2Mn. The Scheil solidification sequence of the Al−3Fe−2Mn alloy under the non-equilibrium solidification conditions was calculated and compared with the results obtained under equilibrium conditions (e.g., under a low cooling rate). Under non-equilibrium conditions, although some primary Al_6M phases may be formed in the early stages of solidification, a two-phase eutectic reaction subsequently occurs, generating the eutectic $Al_6M/\alpha(Al)$ phase. Under

equilibrium conditions, however, the formation of a stable θ phase ($Al_{13}Fe_4$), that is, the primary Al−Fe intermetallic compound, is anticipated.

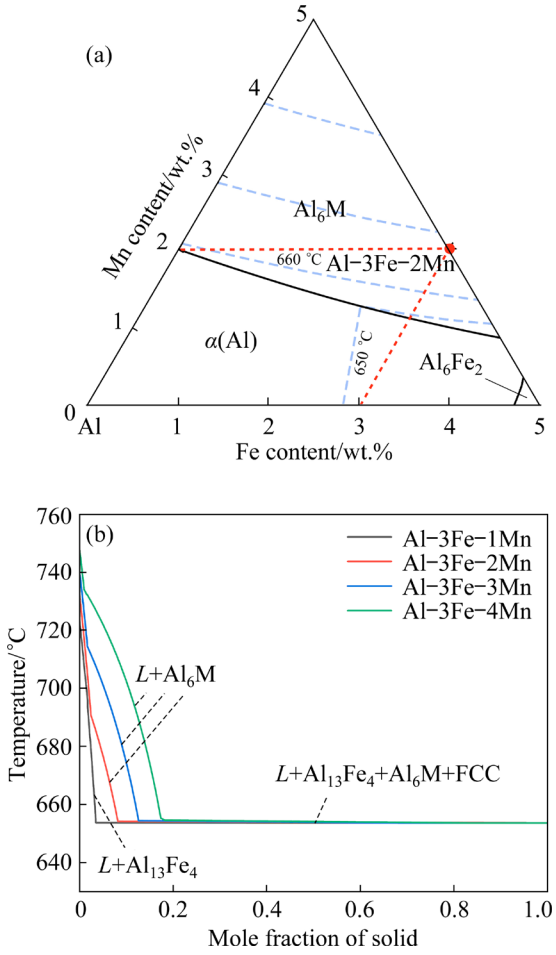

Fig. 2 Calculation result of non-equilibrium liquidus projection in ternary system of Al−Fe−Mn (excluding θ-$Al_{13}Fe_4$ phase) (a); Scheil sequences of Al−3Fe−xMn (x=1, 2, 3 and 4, wt.%) alloys under non-equilibrium solidification conditions (b)

2.2 Materials and methods

With the gas atomization process, pre-alloy powders were synthesized from a combination of Al ingot, Al−20Fe, and Al−Mn master alloys. The morphology of the initial powder, depicted in Fig. 3(a), demonstrates its spherical nature. The individual powder micrographs are shown in Fig. 3(b). Particle sizing conducted with the Malvern UK Zetasizer Nano ZS identified the average size of particles (volume-weighted basis) to be 44 μm, with a distribution ranging from 2.13 to 144 μm, detailed in Fig. 3(c). The chemical composition of the Al−Fe−Mn alloy powders, as well as that of the specimens produced by L-PBF, was determined through inductively coupled plasma-atomic emission spectrometry (ICP-AES), with the findings detailed in Table 1.

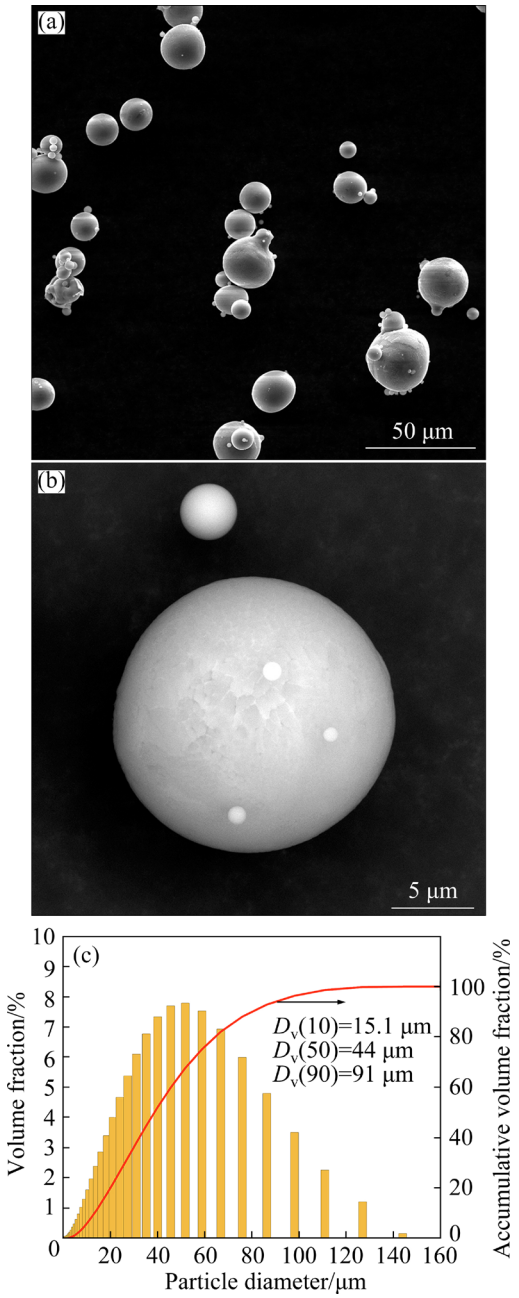

Fig. 3 Powder morphology (a); Microstructure of powder particles (b); Particle size distribution (c)

Table 1 Chemical composition of powder and L-PBF printed samples (wt.%)

Sample	Fe	Mn	Al
Powder	2.72	1.96	Bal.
L-PBF	2.73	1.92	Bal.

Subsequently, the fabrication of Al−Fe−Mn alloy specimens was conducted using LASERADD DiMetal−150 L-PBF system, under a protective

argon atmosphere. This system was equipped with a 500 W fiber laser, delivering a beam with a focus diameter of 90 μm. Through the careful optimization of process parameters, the island scanning strategy was applied on samples with dimensions of 10 mm×10 mm×10 mm, aimed at microstructural characterization (Fig. 4(c)), and 15 mm×75 mm×30 mm for assessing mechanical performance (Fig. 4(b)). The chosen parameters included laser power of 150−300 W and scanning rate of 400−1200 mm/s, employing a checkerboard pattern with a hatch distance of 0.1 mm. Our objective was to identify a parameter range that could minimize defect formation, such as cracking and porosity. Preliminary results indicated that parameters within this range yielded Al−Fe−Mn samples with relative densities exceeding 94.5%. Furthermore, the scanning direction was alternated by 67° between consecutive layers (N and N+1) to mitigate structural weaknesses (Fig. 4(a)).

The relative density of the L-PBF-fabricated specimens was determined using the Archimedes method. Microstructural and defect analyses were performed with a Leica DM4000M optical microscope and a Nova Nano SEM 230 scanning electron microscope, respectively. Sample etching was achieved using a 5 vol.% HF aqueous solution at room temperature. The phase identification was conducted via X-ray diffraction (XRD) on a D/max2500pc, utilizing Cu K_α radiation (λ=0.154 nm), across a 2θ range of 20°−80°. Electron backscatter diffraction (EBSD) analysis, performed using a FEI Nano Lab 600i SEM, was used to elucidate the crystallographic orientation and distribution. Microhardness measurements were obtained with a microVickers hardness tester (conforming to ASTM E384-08), under a load of 100 g for 15 s. The mechanical performance was measured by an MTS Alliance RT system, with a crosshead rate of 2 mm/min. Finally, the sediment distribution within the alloy was characterized using a JEOL 2100F transmission electron microscope, equipped for high-resolution imaging.

3 Results

3.1 Densification

The densification parameters of Al−3Fe−2Mn powder prepared by laser scanning were evaluated. The relative density of each sample block was measured by Archimedes' principle and using Image-Pro Plus software. Figure 5(a) shows the relationship between the sample density of Al−3Fe−2Mn alloy printed with different parameters and the volumetric energy density (VED). As the VED increases, the density of all L-PBF samples initially increases, but the density tends to decrease at higher VED. This means that the relationship between VED and relative density for each L-PBF alloy has a peak, e.g., the optimal forming parameters. The VED (E_d) is derived from laser scanning parameters such as laser power P (W), the hatch spacing h (mm), scanning rate v (mm/s), and layer thickness t (mm), as shown in Eq. (1):

$$E_d=\frac{P}{vht} \tag{1}$$

Figure 5(b) shows the change of the relative density of samples produced at different scanning rates (v) and the applied laser power (P). Across all applied scanning rates, the relative density of the samples increases with an increase in laser power. It is also found that at the same laser power, higher

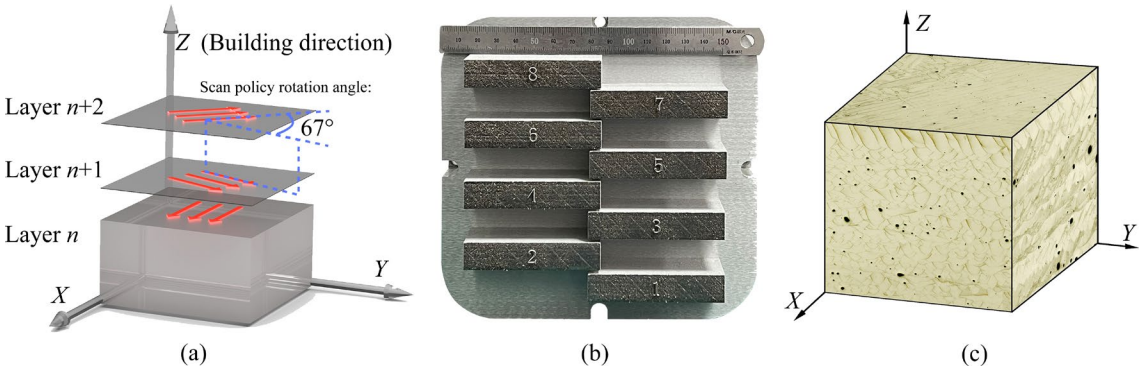

Fig. 4 Scanning strategy of L-PBF printed Al−3Fe−2Mn alloy (a); Printed Al−3Fe−2Mn tensile samples (b); Stereo-metallographic diagram of Al−3Fe−2Mn sample (c)

scanning rates result in high relative densities, indicating that high scanning rates are conducive to the densification of the samples. At high laser power (P=300 W) and low scanning rate (v≤1200 mm/s), dense Al−3Fe−2Mn alloy samples with a relative density higher than 99% can be produced. Figure 6 shows optical micrographs on the XZ plane of Al−3Fe−2Mn samples printed by L-PBF at different VEDs. It can be observed that at VED values between 50 and 70 J/mm^3, the samples exhibit a large number of irregular pores and microcracks, and irregular pores larger than 200 μm can even be observed, which are typically referred to as "process-induced porosity" [33]. This is caused by incomplete melting with insufficient energy supply, leading to a lower relative density of the specimens. As the VED increases, irregular pores and microcracks gradually decrease. When

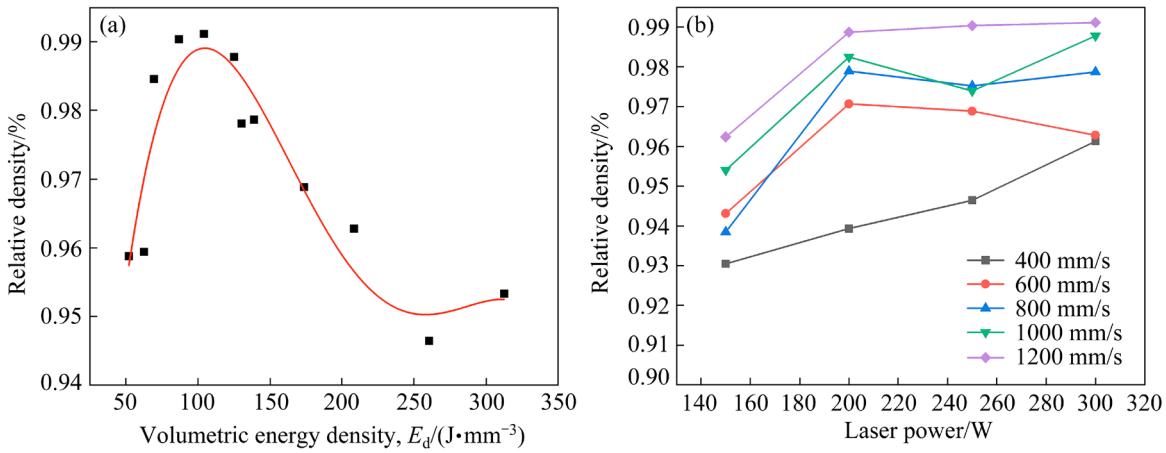

Fig. 5 Relationship between relative density of Al−3Fe−2Mn alloy and VED (a); Diagram of relative density variation and laser power at different scanning rates (b)

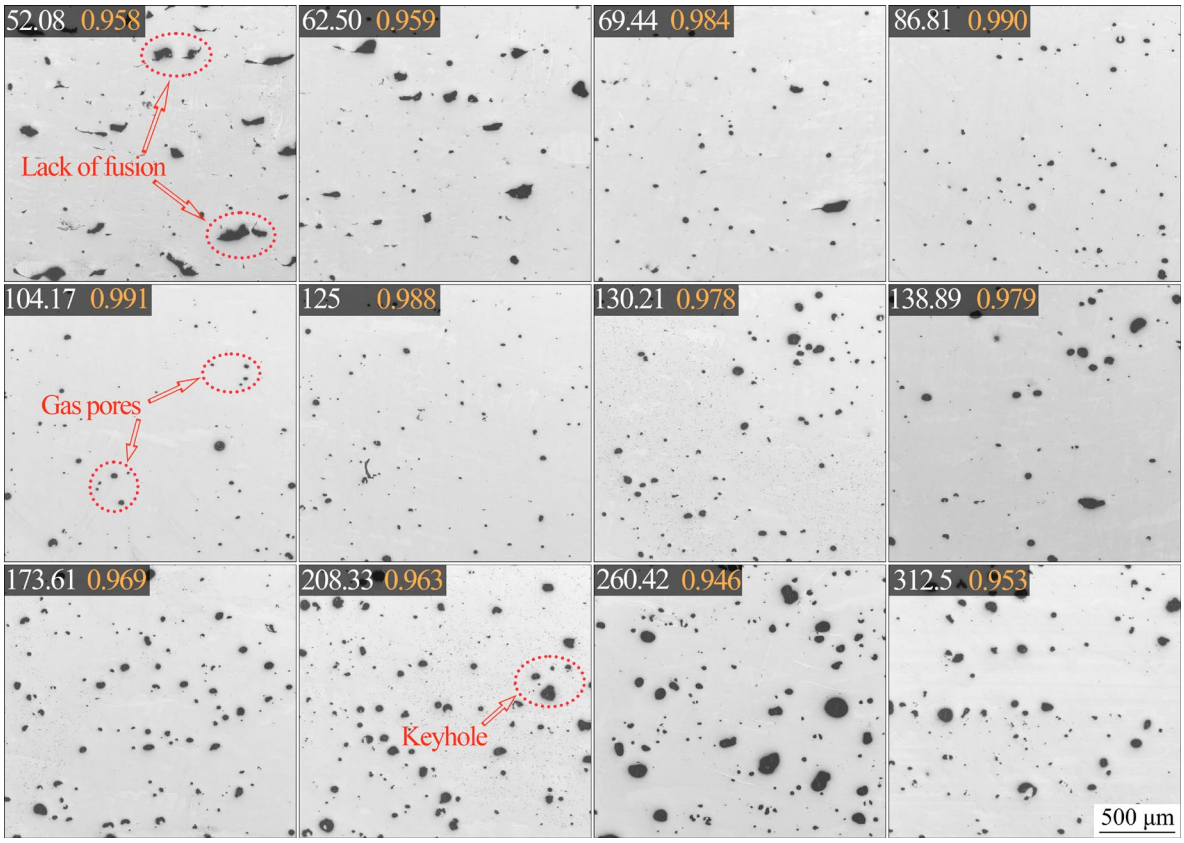

Fig. 6 Metallography of Al−3Fe−2Mn alloy printed by L-PBF at different deposition energy densities (White numbers represent VED (J/mm^3) and orange numbers represent density)

the VED reaches 100−125 J/mm^3, fewer pores can be detected in the samples, and the type of pores changes from irregular to spherical. When the VED is higher than 125 J/mm^3, a keyhole mode of melting is induced, leading to a substantial decrease in the relative density of the sample. Notably, pore formation arises from the vaporization of constituent elements and the entrapment of vapor within the molten pool. The experiment shows that the mechanism of pore formation is closely related to energy input. Furthermore, the red circles in Fig. 6 indicate fusion defects, with some pores containing unmelted alloy powder, suggesting that the laser power is insufficient to fully melt the powder bed [34]. For the L-PBF process, the dynamic viscosity (μ) of the melt pool is related to temperature (T) and can be estimated using Eq. (2) [35]:

$$\mu = \frac{15}{16}\left(\sqrt{\frac{m}{kT}}\gamma\right) \tag{2}$$

where m represents atomic mass, k denotes the Boltzmann constant, and γ represents the surface tension of the melt. It is evident that the temperature of the melt pool depends on the VED. When the VED is below 69.44 J/mm^3, the melt pool temperature remains at a lower level, leading to increased melt viscosity and hindering the diffusion of liquid metal. Moreover, insufficient energy input results in incomplete melting of the metal powder, reducing the wettability and fluidity within the melt pool. These conditions together promote the formation of irregularly shaped pores and corresponding decrease in relative density. When the energy input is increased to 86.81 J/mm^3, the microstructure only shows limited spherical pores. This phenomenon may be caused by the transition in the melting mode of the melt pool from conduction to keyhole, induced by Marangoni convection and thermal input [36,37]. With further increase to 125 J/mm^3, although pores still exist, their density significantly decreases, and the densification is markedly improved, in accord well with Fig. 3(a). This indicates that the presence of pores can be mitigated or even eliminated by fine-tuning the processing parameters.

3.2 Microstructure

In this study, the phase composition of Al−3Fe−2Mn aluminum alloy was analyzed in detail using XRD. The XRD patterns of alloy powder and printed samples with different VEDs are shown in Fig. 7. The spectral analysis reveals significant differences in phase composition under different preparation conditions. The various peaks observed in the spectra correspond to different phases present in the alloy, providing evidence of its microstructural characteristics. Four high-intensity diffraction peaks located at 2θ=38.5°, 45°, 65°, and 78.5° are attributed to (111), (200), (220), and (311) crystal planes of the face-centered cubic (FCC) α(Al) phase, respectively. Other peaks correspond to the orthorhombic Al_6M phases. $Al_{13}Fe_4$, $Al_6(Fe,Mn)$, and $Al(Fe,Mn)_3$ intermetallic phases indicate the formation of secondary phases

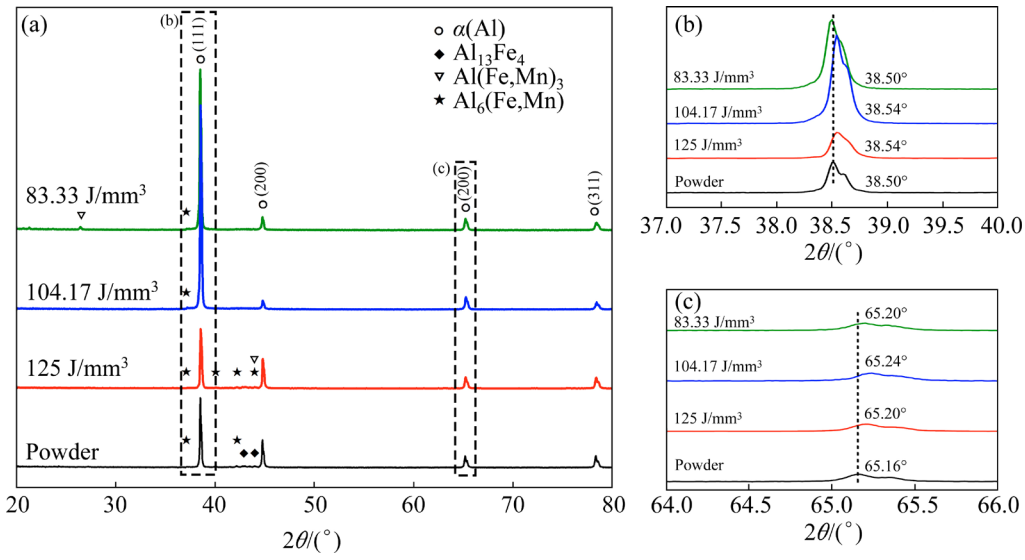

Fig. 7 XRD patterns of printed samples at different VEDs and alloy powders

during the printing process. The orthogonalized Al_6M indicates the microstructure changes caused by the rapid solidification in the L-PBF process. This is also influenced by the gas atomization techniques used to prepare the powder. The formation of these phases is usually associated with the strengthening of aluminum alloys but may also reduce their ductility if present in large quantities. XRD patterns under different VEDs reveal the impact of printing process parameters on phase formation. As the energy density increases from 83.33 to 125 J/mm³, significant changes occur in the intensity and width of the peaks. Particularly at higher energy densities, the relative intensity increase of intermetallic peaks indicates a higher degree of these phases. This is likely because the higher energy input promotes more extensive phase growth. Furthermore, this may also indicate the effect of solidification rate variations on the mechanical performance of the specimens. The comparison of the diffraction peaks in the printed state with those in the powder provides deep insight into phase transitions induced by the AM process. The variation in peak width and intensity in the printed state, relative to the powder, suggests that the microstructure of the printed specimens is changed due to the inherent rapid cooling rate of the L-PBF technology, such as grain refinement and the development of residual stresses.

Figures 8(a−c) present the microstructural characteristics of Al−3Fe−2Mn alloy samples prepared by the L-PBF which are cross-sectional images perpendicular to the build direction (*Z* direction). In the low-magnification backscattered electron (BSE) image of Fig. 8(a), the billet alloy sample prepared under optimized laser conditions (P=300 W and v=1200 mm/s) exhibits a highly uniform dense structure. The melt pool structure is visible, with localized melting and solidification areas forming a continuous semi-cylindrical pattern. No solidification cracks or other obvious metallurgical defects are observed, indicating that the optimized parameters can achieve effective control of melting and solidification. This fine melt pool structure not only demonstrates the high precision of the L-PBF process but also provides an excellent foundation for the material's performance. Columnar grain regions are found, which grow along the constructed direction, likely due to the local temperature gradient differences caused by laser irradiation, leading to the formation of grain orientation.

The microstructure of materials printed by L-PBF is influenced by the thermal boundary evolution of the melt pool [38]. As observed from Fig. 8(a), a cell structure with a width of several micrometers is formed at the melt pool boundary, where the cooling rate is high and the temperature gradient is low. This cell structure is coarser compared with the finer microstructure observed

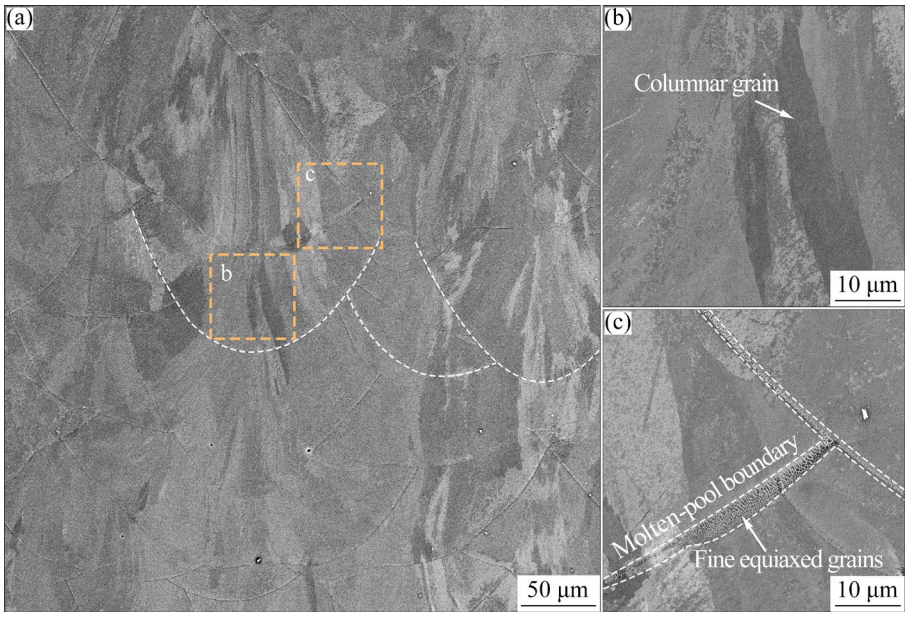

Fig. 8 SEM image of Al−3Fe−2Mn sample at low magnification (a); SEM image of columnar grain of sample at high magnification (b); SEM images of fine equiaxed grain region of sample at high magnification (c)

within the melt pool. On the other hand, elongated columnar grain structures are observed (Fig. 8(b)) inside the melt pool, where the cooling rate is low and the temperature gradient is high. Notably, as indicated in the SEM images, the contour of the melt pool is less distinct, with very narrow melt pool boundaries (Fig. 8(c)), and the fine grain zone at the melt pool boundary presents a honeycomb structure with a size of several micrometers. Furthermore, the fine grain zone occupies a smaller proportion of the entire melt pool, indicating that the material primarily grows into columnar grains during the L-PBF process. This microstructural characteristic may be one of the reasons why the alloy exhibits poor mechanical performance at room temperature but high performance at high temperature.

The SEM images in Fig. 9 display the fracture surface of the Al−3Fe−2Mn alloy after tensile testing at room temperature (24 °C) and at high temperature (200 and 300 °C). As shown in Figs. 9(a, e, i), the well-arranged band pattern on the macro fracture spans 100−200 μm. This indicates that the fracture path is related to the laser scanning strategy in the L-PBF process, and the fracture mainly occurs at the melt pool boundary. This feature is consistent with the microstructural anisotropy induced by L-PBF and the local variation in mechanical performance at the melt pool boundaries. At the microscopic scale, the ductile fracture texture features of dimples confirm the intrinsic toughness of the material. The size of these dimples is about a few micrometers (Figs. 9(d, h, l), representing common mechanism of microvoid coalescence in the ductile fracture of aluminum alloys. Moreover, the persistence of these patterns at high temperature (200 and 300 °C) may reveal the microstructural characteristics of the alloy, possibly due to the presence of Al and Mn, as the formation of Al_6M (M=Fe, Mn) precipitates that do not dissolve easily at high temperature, maintaining a certain degree of brittleness. L-PBF process parameters, such as laser power, scanning rate, and hatch spacing, significantly influence the grain structure and phase distribution, thus leading to the fracture characteristics observed. However, the presence of the aforementioned “river patterns” on the fracture surfaces at all three temperature points suggests the coexistence of cleavage planes and mechanisms of ductile and brittle fracture,

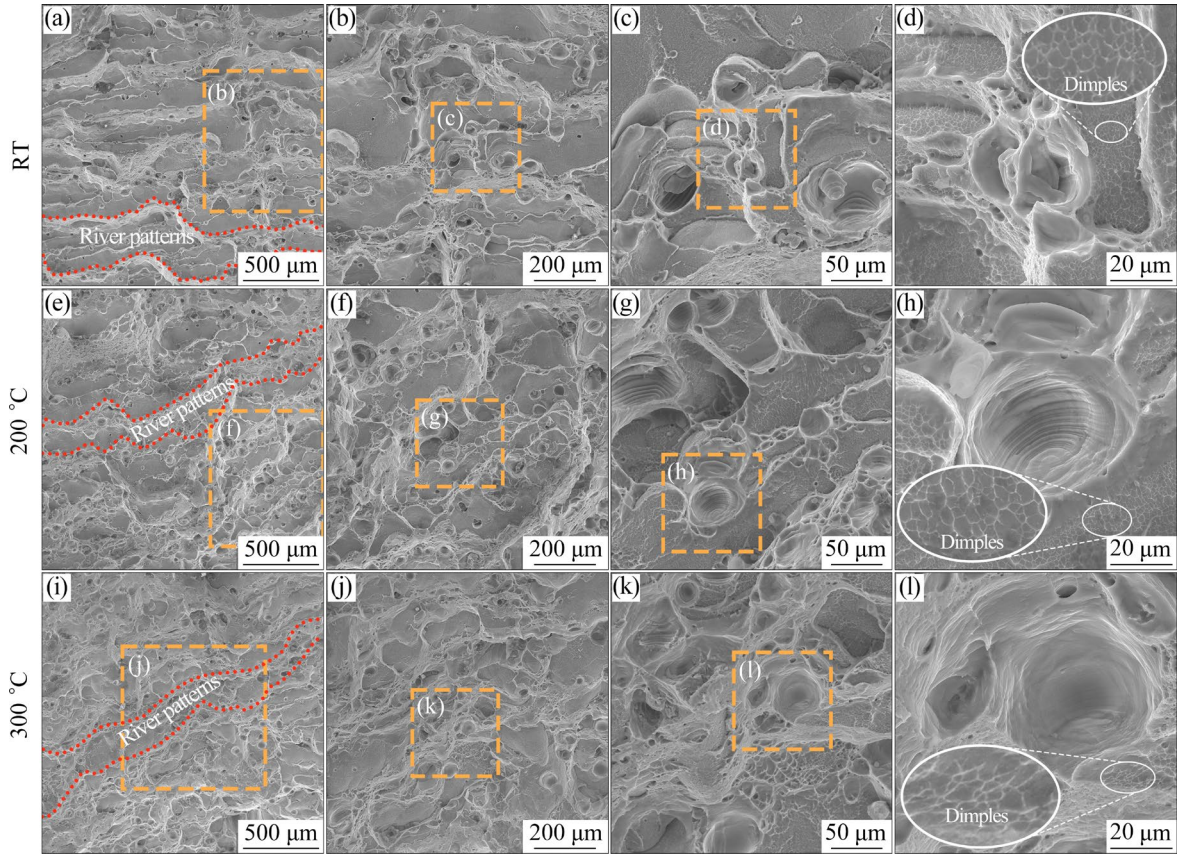

Fig. 9 SEM images for fracture morphologies of Al−3Fe−2Mn at different temperatures

especially at room temperature. These findings are consistent with research on high-performance aluminum alloys processed by AM technology, where fracture behavior is closely related to thermal history and resulting microstructural heterogeneity. To further explore the fracture characteristics, precipitate phases and secondary phases as microstructural constituents are considered. The interactions between these microstructural features and the observed fracture surfaces will be focal points for material's design and optimization to obtain enhanced mechanical performance.

Figure 10 presents high-angle annular dark-field (HAADF) scanning transmission electron microscopy (STEM) images, detailing the contour and internal microstructure of the melt pool formed by L-PBF. As illustrated in Fig. 10(a), the periphery of the melt pool is characterized by cellular structures spaced hundreds of nanometers apart, consistent with the coarser honeycomb-like sub-cellular microstructure shown in Fig. 6(c). Specifically, Fig. 10(b) shows the formation of fine cellular/dendritic structures within the melt pool, which is attributed to the inherent rapid solidification of the L-PBF process. Inside the melt pool, spherical to slightly elongated intermetallic phases can be observed, ranging from tens to hundreds of nanometers (Figs. 10(b, c)). These phases are primarily composed of Fe and Mn elements and are evenly distributed which are crucial to the strengthening mechanism of the alloy. Selected area electron diffraction (SAED) patterns near the melt pool edge (Fig. 10(d)) display a ring structure, indicating randomly oriented polycrystalline intermetallic phases. The most pronounced ring is associated with the (312) crystal plane of the orthorhombic Al_6M intermetallic phase. Moreover, the SAED patterns also show bright spots on a diffusive background corresponding to the fundamental reflections of the α(Al) matrix (FCC), consistent with the [011] α(Al) beam direction. The comprehensive analysis combining HAADF-STEM, SAED, and energy dispersive spectroscopy (EDS) mapping elucidates the microstructural and crystallographic characteristics of the Al−3Fe−2Mn alloy processed by L-PBF.

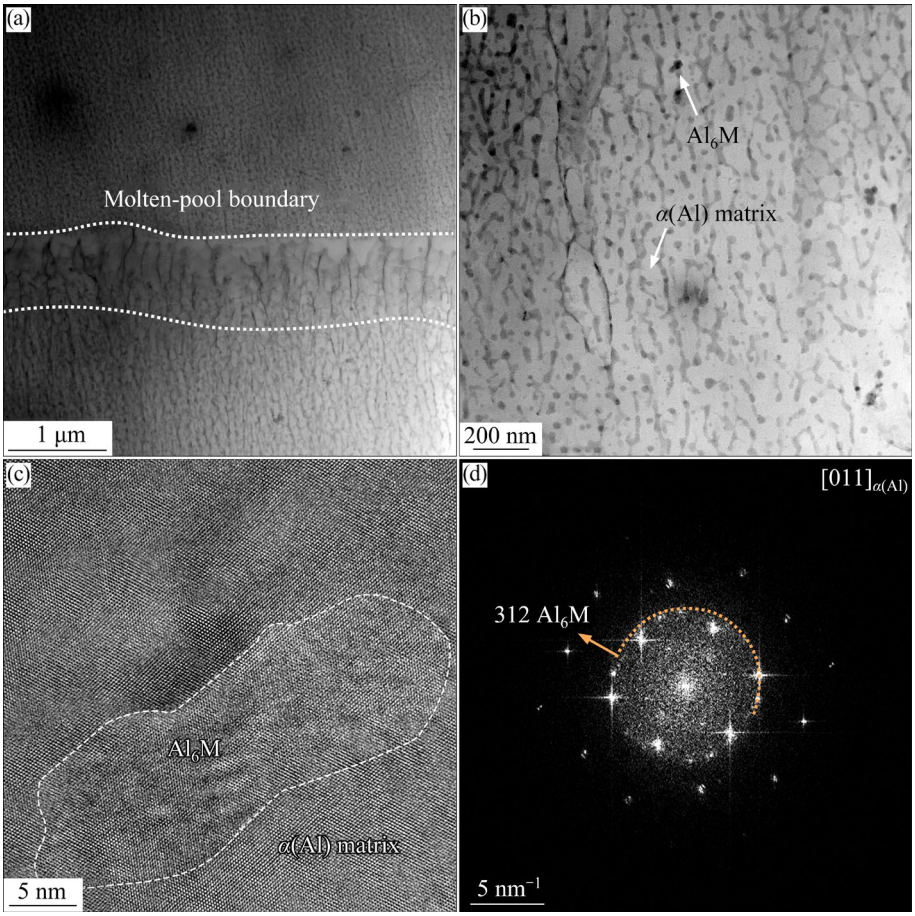

Fig. 10 Bright-field (BF)-STEM image of cell microstructure around molten pool boundary (a); BF-STEM image of nano-sized particles distributed in molten pool (b); HRTEM image (c) and SAED pattern (d) of Al_6M particles

Figure 11 displays STEM images of the microstructure inside the melt pool and the corresponding energy dispersive spectroscopy (EDS) mappings. Microstructure is characterized by fine sub-cellular structures. Higher magnification HAADF-STEM image in Fig. 11(b) and the corresponding EDS mappings show that Al is uniformly distributed throughout the matrix, while Fe and Mn are distinctly segregated into fine intermetallic phases. Quantitative EDS point analysis was carried out at different locations in the sample to measure the solute content of Fe and Mn. Representative results for the matrix and nanocrystalline grain of the sample are shown in Fig. 11(c). In the intergranular regions, the contents of Fe and Mn are particularly high, suggesting that Al−Fe and Al−Mn phases may be formed during the solidification process due to local solute enrichment, as indicated by the Al_6M(Fe,Mn) phase in Fig. 10(d). The presence of these intermetallic compounds is crucial as they can significantly affect the mechanical performance of the alloy by potentially enhancing strength and hardness.

In the L-PBF process, an energy-dense laser beam melts the metal powder, which is then rapidly cooled to form a solid. This rapid cooling process typically leads to the formation of fine grains and can produce significant grain orientation heterogeneity. Figure 12 presents the electron backscatter diffraction (EBSD) data of the Al−3Fe−2Mn alloy, comprehensively showcasing microstructural and crystallographic characteristics of the alloy.

In Fig. 12(a), the EBSD orientation color map of the alloy reveals varied microstructures with significant changes in grain orientation. The formation of grains is uneven, indicating complex thermal gradients and solidification dynamics during the L-PBF process. Notably, grains mainly have an elongated columnar shape and stretch along the building direction, indicating a typical L-PBF directional heat dissipation. The columnar grains, surrounded by high-angle grain boundaries (misorientation angles large than 15°), are elongated

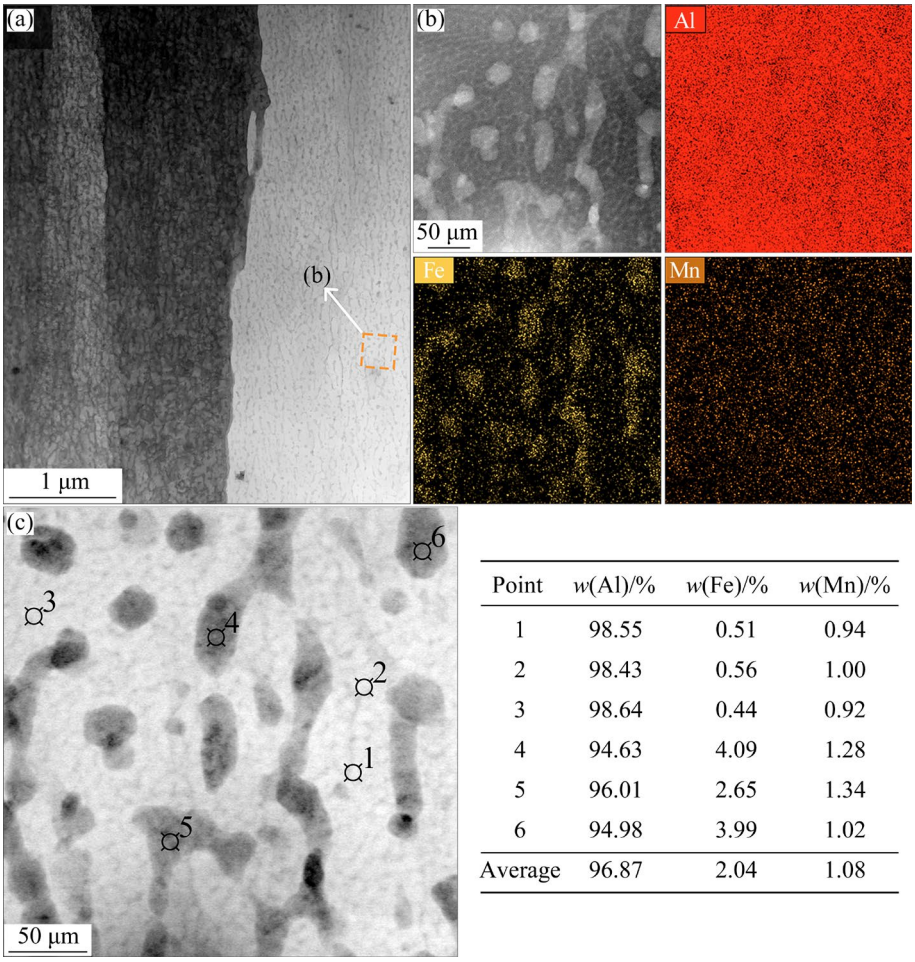

Point	w(Al)/%	w(Fe)/%	w(Mn)/%
1	98.55	0.51	0.94
2	98.43	0.56	1.00
3	98.64	0.44	0.92
4	94.63	4.09	1.28
5	96.01	2.65	1.34
6	94.98	3.99	1.02
Average	96.87	2.04	1.08

Fig. 11 HAADF-STEM image of crystal cells in molten pool (a); HAADF-STEM image of nanoscale particles and corresponding EDS mappings (b); HAADF-STEM image and corresponding EDS point analysis results (c)

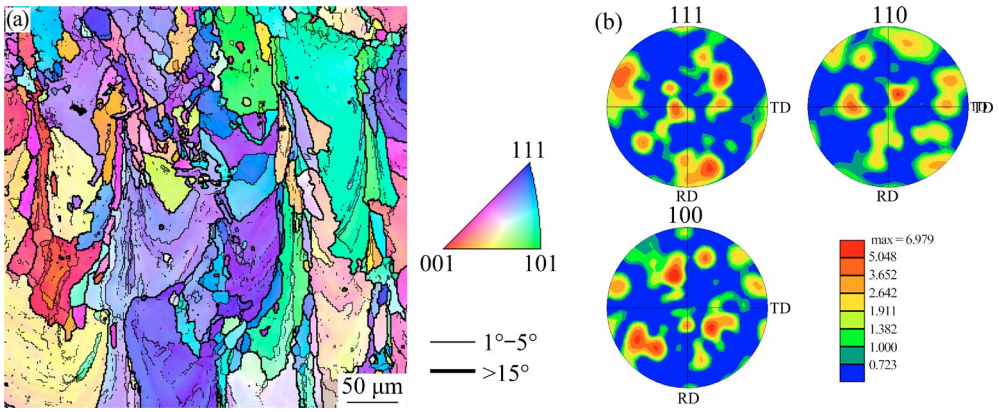

Fig. 12 EBSD orientation color diagram of α(Al) (FCC) in Al−3Fe−2Mn sample manufactured by L-BPF (P=300 W, and v=1200 mm/s) (a); Representative pole figures of low indices (b)

in the building direction and contain a relatively higher number of low-angle grain boundaries (misorientation angles less than 15°) within the elongated grains, which could be attributed to the inherent rapid cooling rates in the L-PBF process. Figure 12(b) shows the pole figures (111, 100, 110) of low refractive indices for the Al−3Fe−2Mn alloy, revealing the material's crystal texture. The intensity distribution in the polar maps is relatively dispersed, with multiple peaks rather than a single dominant orientation, likely as a result of the processing parameters leading to more randomized grain orientation. However, some intensity clusters indicate a degree of preferred grain orientation, although not as pronounced as observed in materials with different parameters or a single major grain growth direction.

The EBSD result suggests that due to rapid solidification, the material exhibits a complex multi-orientational organization. Despite the high cooling rates, the presence of elongated grains and discernible grain textures is noteworthy. These findings are helpful in understanding the micro-structural evolution of the Al−Fe−Mn alloys produced by AM and influence the optimization of processing parameters to achieve the desired mechanical performance.

3.3 Mechanical performance

Figure 13 reveals the trend of hardness variation of L-PBF Al−3Fe−2Mn parts with the change in VED. The result shows that the hardness experiences a pattern of initial increase, followed by a decrease, and then an increase again, as the VED increases. At VED below 100 J/mm^3, the gradual

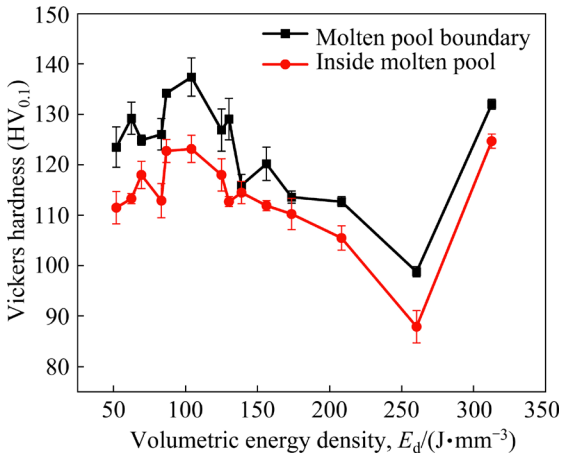

Fig. 13 Relationship between Vickers hardness and VED of L-PBF Al−3Fe−2Mn alloy

increase in hardness could be attributed to insufficient early energy input leading to incomplete fusion, where the formation of pores and unfused particles weakens the overall hardness of the material. At 104.6 J/mm^3, the sample reaches its maximum density (as shown in Fig. 5(a)) and the highest hardness of HV 137.4. However, when VED is in the range of 100−260 J/mm^3, hardness shows a decreasing trend, possibly because the excessive energy density causes keyhole defects. When the VED exceeds 260 J/mm^3, the sharp increase in hardness could be attributed to the formation of supersaturated solid solutions or the formation of non-equilibrium phases due to rapid cooling. Nevertheless, the samples at high energy densities have lower density (Fig. 5(a)) and poor formability. Additionally, there is a significant difference in hardness between the boundaries and interiors of the melt pool, because the rapid cooling at the melt pool boundaries leads to the formation

of fine-grained zones and Al_6M (M=Fe, Mn) metastable phases, whereas the interior of the melt pool experiences grain growth due to slow cooling rates.

Figure 14(a) displays the tensile testing results of the heat-resistant Al−3Fe−2Mn alloy at various temperatures. These tests were designed to evaluate the high-temperature mechanical performance of the alloy. At room temperature, the alloy exhibits outstanding mechanical performance, with yield strength and tensile strength reaching 286 and 360 MPa, respectively, and ductility at 3.2%. However, as the temperature increases to 200 and 300 °C, both yield strength and tensile strength show a downward trend. The tensile strength is 295 MPa at 200 °C, and the ductility increases to 3.8%. At 300 °C, the tensile strength is reduced to 230 MPa, and the ductility is further increased to 4.9%. This change in performance is likely due to the coarsening of nano-sized metastable phases Al_6M (M=Fe, Mn) within the alloy and the transformation of metastable phases to $Al_{13}Fe_4$ at high temperature. Moreover, high temperature may activate internal slip systems and promote dynamic recrystallization, reducing the material's resistance to deformation. Notably, although the yield strength and tensile strength of the alloy slightly decrease with increasing testing temperature, this reduction is not significant, demonstrating its excellent strength retention ability in high-temperature environments. At high temperature, the Al−3Fe−2Mn alloy shows remarkable strength stability. As revealed in Fig. 14(b), at a working temperature of 200 °C, the yield strength retention rate of the alloy reaches up to 92.7%, while the tensile strength maintains 81.9%. With further increasing the temperature to 300 °C, the retention rates of yield strength and tensile strength of the alloy still reach 73.4% and 63.9%, respectively, demonstrating its reliability and superior performance in high-temperature applications.

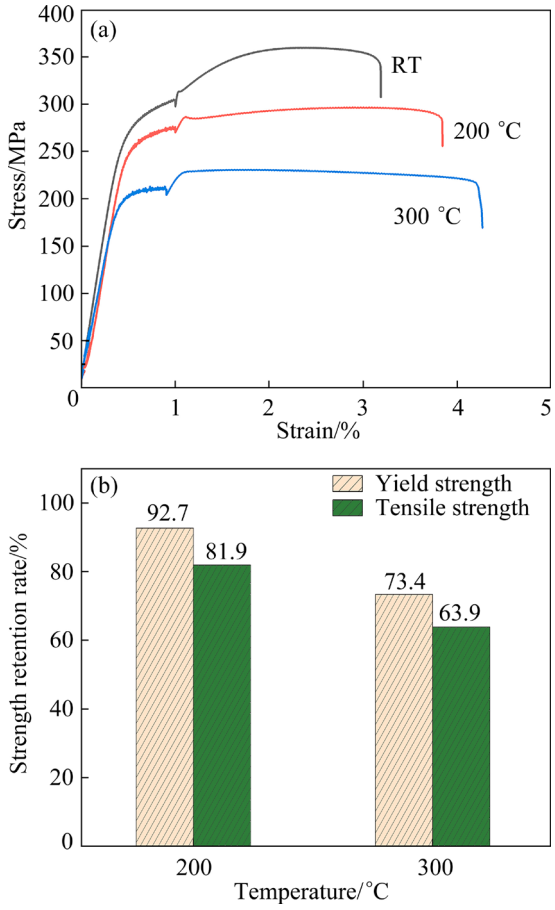

Fig. 14 Stress−strain curves of Al−3Fe−2Mn at different temperatures (a); Comparison of retention rates of yield strength and tensile strength at 200 and 300 °C (b)

4 Discussion

4.1 Densification and composition design of alloys

In this study, to ascertain the maximum solubility of Fe in Al alloys, laser remelting experiments were conducted on cast alloys with varying iron contents using fixed laser parameters, and the morphological changes of the melt pool were recorded (Fig. 1(a)). Further, by employing the non-equilibrium liquidus projection of the Al−Fe−Mn ternary alloy system and the Scheil solidification model (as illustrated in Fig. 2), the maximum content of manganese in the ternary alloy was determined alloys and ultimately confirmed the composition of Al−3Fe−2Mn alloy. Additionally, in this study, the feasibility of printing the Al−3Fe−2Mn alloy using L-PBF technology and its correlation with the alloy composition were explored. The specific printing process and phenomena are detailed in Fig. 15(a), with Fig. 15(b) displaying the post-printing melt pool morphology. To accommodate variations in alloy density induced by different printing parameters (Fig. 15(c)), meticulous parameter optimization was undertaken, establishing optimal laser parameters for achieving full densification of the Al−3Fe−2Mn alloy: a laser power of 300 W and a scanning rate of 1200 mm/s. Through these optimizations, samples with a density exceeding 99% were successfully fabricated. Data analyses shown in Figs. 3 and 7 indicate that

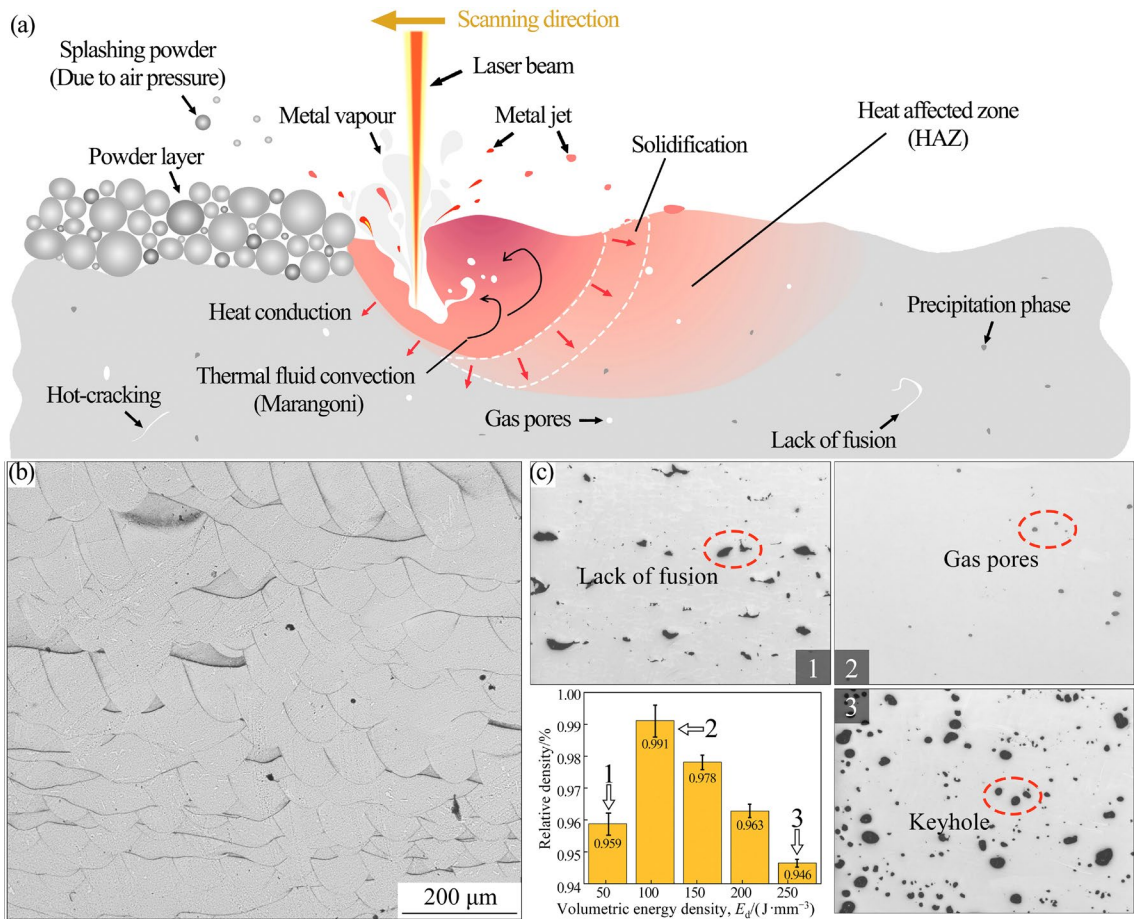

Fig. 15 Schematic diagram of L-PBF printing process and its related phenomena (a); Cross-section topography of alloy melt pool (b); Defects morphologies and variations in relative density of alloy with different printing parameters (c)

the printability of the alloy is closely related to the selected printing parameters, as validated in the study of Al−Fe binary alloy [28]. Moreover, in-depth analysis reveals that the printability of the alloy is not only significantly influenced by the printing parameters but also directly constrained by the contents of Fe and Mn. Guided by the non-equilibrium liquidus projection, maximizing the contents of Fe and Mn not only enhances the density of the alloy but also effectively prevents excessive porosity and crack formation. Furthermore, laser scanning of the cast alloys effectively inhibits the formation of coarse intermetallic phases with high volume fraction at high temperature, a strategy crucial for controlling crack formation during the L-PBF process [39].

4.2 Solidification microstructure

Through a series of precise material characterizations, it is found that the microstructure of the molten pool in the high-density Al−3Fe−2Mn alloy samples, fabricated by L-PBF technology, predominantly features a mixture of columnar and a minor fraction of equiaxed grains. This structure implies that the melt pool's contour is not readily identifiable under SEM. Notably, within the melt pool and its boundary regions, an abundance of nanoscale strengthening phases, metastable Al_6Mn and Al_6Fe phases, are observed. The emergence of these phases significantly contributes to the strengthening of material. Thus, the strengthening of high-strength, heat-resistant aluminum alloys principally relies on fine-grain strengthening and the Orowan strengthening effect of nanoscale precipitates. The L-PBF process facilitates rapid solidification in the aluminum matrix, promoting a substantial solid solution of Fe and Mn, while concurrently encouraging the formation of spherical and reticular nanoscale Al_6Mn and Al_6Fe phases. The distribution of these nanoscale intermetallic compounds within the aluminum matrix notably impedes grain boundary migration and dislocation movement through a pinning effect, thereby stabilizing the α(Al) grain structure and significantly

enhancing the strength of the Al−Fe−Mn alloy. Experimental data demonstrate that, compared with Al−2Fe and Al−2.5Fe alloys [20,40], the Al−3Fe−2Mn alloy exhibits higher tensile strength and yield strength. This phenomenon can be attributed to the increased Fe content leading to the formation of Al_6Fe phases, thus improving the material's performance at room temperature and high temperature. EDS results, as shown in Fig. 12, reveal that Fe is primarily concentrated within nanoscale particulate phases, while Mn distribution is comparatively more uniform. The addition of Mn not only increases the alloying element concentration in the α(Al) solid solution but also acts as a nucleating agent, further promoting the formation of more Al_6Mn and Al_6Fe nanophases during the rapid solidification process of L-PBF. Additionally, the substitution of some Mn atoms in place of Fe in the Al_6Fe phase stabilizes Al_6Mn and Al_6Fe phases, effectively suppressing the formation of the θ($Al_{13}Fe_4$) phase within the Al−Fe−Mn ternary alloy system. Consequently, as depicted in Fig. 7, the formation of the θ phase is not observed in L-PBF Al−3Fe−2Mn alloy.

4.3 Mechanical performance

Under ambient conditions, Al−3Fe−2Mn alloys fabricated via L-PBF technology demonstrate exceptional mechanical performance, including a tensile strength of 360 MPa and an elongation of 3.2%. At high temperature of 200 and 300 °C, the tensile strength of the alloy decreases to 295 and 230 MPa, respectively. Compared with similar aluminum alloys under similar high-temperature conditions (Fig. 16), the Al−3Fe−2Mn alloy exhibits superior strength retention capability. The outstanding tensile strength exhibited by the alloy at high temperature can be attributed to the refinement of its dual-phase microstructure, consisting of α(Al) and Al_6M, which demonstrates significant thermal stability even at temperature up to 300 °C. Notably, the nanoscale Al_6Mn precipitates distributed in a network within the α(Al) solid solution markedly increase the resistance to dislocation motion, as illustrated in Fig. 10(b). In the Al−Fe binary system, the nanoscale metastable Al_6Fe phase dissolves at high temperature, leading to the formation of coarse θ stable phases [24,41], thereby significantly reducing the alloy's strength. However, from a thermodynamic perspective, the introduction of Mn stabilizes the Al_6Fe phase within the α(Al) matrix, thereby facilitating the formation of a dual-phase microstructure of α(Al) and Al_6Mn, which remains stable even under high-temperature conditions. Consequently, the addition of Mn not only promotes the refinement of the α(Al) and Al_6Mn dual-phase structure but also enhances the thermal stability. The Al−3Fe−2Mn alloy demonstrates commendable high-temperature performance, suggesting broad application potential.

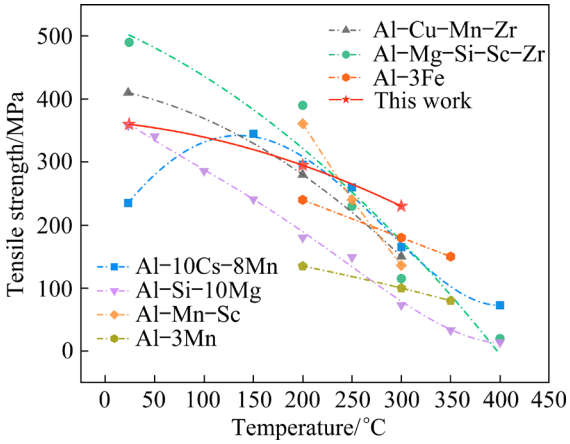

Fig. 16 Tensile strength of L-PBF Al−3Fe−2Mn alloy as function of test temperature, compared with results of other L-PBF aluminum alloys [18,42−46]

5 Conclusions

(1) Optimal L-PBF parameters (P=300 W, v≤1200 mm/s) are identified, achieving a relative density exceeding 99%. At lower VED, the energy supplied is insufficient for complete powder melting, leading to defects. Increasing VED reduces porosity and cracking, optimizing relative density at 99.1%. However, exceeding 104.17 J/mm³ introduces significant keyhole porosity. Tailoring alloy compositions and refining the printing parameters can mitigate these defects.

(2) The microstructural examination of the L-PBF fabricated Al−3Fe−2Mn samples reveals distinctive multi-scan melt pools, created by localized melting and rapid solidification. The melt pool boundaries display subtle, fine-grained regions. The α(Al) matrix contains columnar grains (5.1 μm in width, and 68.6 μm in length) and uniformly dispersed Al_6Fe intermetallic nanoparticles (<60 nm) within the melt pools.

(3) XRD analysis predominantly identifies the Al_6M phase, with the absence of the $Al_{13}Fe_4$ phase

in the substrate of the printed components. Electron probe microanalysis, supplemented by energy dispersive X-ray analysis, reveals a significant accumulation of Fe and Mn in the Al_6M phase within the melt pools, confirming the substantial precipitation of both Al_6Fe and Al_6Mn as demonstrated in the transmission electron microscopy image. These elements are crucial for enhancing the alloy's high-temperature strength through mechanisms such as solid solution strengthening, precipitation hardening, and grain boundary strengthening.

(4) The alloy exhibits a tensile strength of ~360 MPa at room temperature, reducing to 295 MPa at 200 °C and 240 MPa at 300 °C. Despite the strength decreases at high temperature, the Al−3Fe−2Mn alloy demonstrates superior strength retention compared with other L-PBF aluminum alloys.

CRediT authorship contribution statement

Jun-sheng CHEN: Investigation, Methodology, Writing – Origin draft, Writing − Review & editing; **Ji-bing CHEN:** Investigation, Conceptualization, Funding acquisition, Supervision, Writing – Review & editing; **Qian-yu SHI:** Investigation; **Yue-ting WANG:** Data curation, Data analysis; **Xi-zhen XIA:** Supervision, Writing – Review & editing; **Rui-di LI:** Supervision, Writing – Review & editing, Funding acquisition.

Declaration of competing interest

The authors declare that they have no known competing financial interests or personal relationships that could have appeared to influence the work reported in this paper.

Acknowledgments

This work was supported by the National Natural Science Foundation of China (No. U21B2073), and the Science and Technology Project of the Science and Technology Department of Hubei Province, China (No. 2022EHB020).

References

[1] ROMETSCH P A, ZHU Yu-man, WU Xin-hua, HUANG Ai-jun. Review of high-strength aluminium alloys for additive manufacturing by laser powder bed fusion [J]. Materials & Design, 2022, 219: 110816.

[2] HE Pei-dong, WEBSTER R F, YAKUBOV V, KONG Hui, YANG Qin, HUANG Shu-ke, FERRY M, KRUZIC J J, LI Xiao-peng. Fatigue and dynamic aging behavior of a high strength Al-5024 alloy fabricated by laser powder bed fusion additive manufacturing [J]. Acta Materialia, 2021, 220: 117276.

[3] LIU Tian-shu, CHEN Peng, QIU Feng, YANG Hong-yu, JIN N T Y, CHEW You-xiang, WANG Di, LI Rui-di, JIANG Qi-quan, TAN Chao-lin. Review on laser directed energy deposited aluminum alloys [J]. International Journal of Extreme Manufacturing, 2024, 6: 022004.

[4] LI Shuang-shuang, YUE Xin, LI Qing-yuan, PENG He-li, DONG Bai-xin, LIU Tian-shu, YANG Hong-yu, FAN Jun, SHU Shi-li, QIU Feng, JIANG Qi-quan. Development and applications of aluminum alloys for aerospace industry [J]. Journal of Materials Research and Technology, 2023, 27: 944−983.

[5] SING S L, YEONG W Y. Laser powder bed fusion for metal additive manufacturing: Perspectives on recent developments [J]. Virtual and Physical Prototyping, 2020, 15(3): 359−370.

[6] LUO Ya-jun, ZHANG Wei-dong, PENG Fei, LIU Sheng, LI Zhong-tao, WU Zheng-gang. Temperature dependence of mechanical properties of equiatomic NiCoCr medium-entropy alloy printed by selective laser melting [J]. Transactions of Nonferrous Metals Society of China, 2024, 34: 1547−1557.

[7] LIU Zhuang-zhuang, ZHOU Qi-hang, LIANG Xiao-kang, WANG Xie-bin, LI Gui-chuan, VANMEENSEL K, XIE Jian-xin. Alloy design for laser powder bed fusion additive manufacturing: A critical review [J]. International Journal of Extreme Manufacturing, 2024, 6(2): 022002.

[8] CHEN Jun-sheng, CHEN Ji-bing, WANG Hong-ze, HE Liang, HUANG Bo-yang, SASAN D, PAULO B. Fabrication and development of mechanical metamaterials via additive manufacturing for biomedical applications: A review [J]. International Journal of Extreme Manufacturing, 2025, 7: 012001.

[9] KIMURA T, NAKAMOTO T, OZAKI T, MIKI T, MURAKAMI I, HASHIZUME Y, TANAKA A. Microstructural development and aging behavior of Al−Cr−Zr heat-resistant alloy fabricated using laser powder bed fusion [J]. Journal of Materials Research and Technology, 2021, 15: 4193−4207.

[10] TANG Hao, GENG Yao-xiang, GAO Chao-feng, XI Xiao-ying, ZHANG Jian-tao, XIAO Zhi-yu. Microstructure evolution and mechanical properties of high-performance Al−Mn−Mg−Sc−Zr alloy fabricated by laser powder bed fusion [J]. Transactions of Nonferrous Metals Society of China, 2024, 34: 1413−1426.

[11] JI Kai-hua, CLARKE A J, McKEOWN J T, KARMA A. Microstructure development during rapid alloy solidification [J]. MRS Bulletin, 2024, 49(6): 556−567.

[12] WANG Zi-hong, ZENG Ling-Guo, LIN Xin, WANG Jing-feng, FENG Zhe, DANG Cong, LI Hong-yun, WANG Yan-fang, HUANG Wei-dong. Microstructural evolution and strengthening mechanisms of additively-manufactured Al−Mg−Sc−Zr alloys: Laser directed energy deposition versus laser powder bed fusion [J]. Journal of Alloys and Compounds, 2024, 985: 173946.

[13] WANG Wen-yuan, XU Yi-fan, DEGUCHI M, TAKATA N, SUZUKI A, KOBASHI M, KATO M, MITSUHARA M, NAKASHIMA H. Thermal stability of refined Al_6(Fe,Mn)

phase formed in laser powder bed fusion process [J]. Journal of Alloys and Compounds, 2024, 992: 174593.

[14] BAHL S, PLOTKOWSKI A, SISCO K, LEONARD D N, ALLARD L F, MICHI R A, POPLAWSKY J D, DEHOFF R, SHYAM A. Elevated temperature ductility dip in an additively manufactured Al−Cu−Ce alloy [J]. Acta Materialia, 2021, 220: 117285.

[15] DENG Jun-wang, CHEN Chao, LIU Xiao-chun, LI Yun-ping, ZHOU Ke-chao, GUO Sheng-min. A high-strength heat-resistant Al−5.7Ni eutectic alloy with spherical Al_3Ni nano-particles by selective laser melting [J]. Scripta Materialia, 2021, 203: 114028.

[16] XU Jing-Yu, ZHANG Cheng, LIU Li-Xue, GUO Rong, SUN Ming-Jun, LIU Lin. Achieving high strength in laser powder-bed fusion processed AlFeCuZr alloy via dual-nanoprecipitations and grain boundary segregation [J]. Journal of Materials Science & Technology, 2023, 137: 56−66.

[17] ZHAO Jun-ren, LEE Liang-yan, CHANG K C, HUNG Fei-yi. A novel two-stage heat treatment with medium-temperature aging influence on microstructure, $Al_3(Sc,Zr)$ nanoprecipitation, and application properties, enhancing selective laser melting of Al−Mg−Sc−Zr alloy [J]. Nanomaterials, 2022, 12(12): 2078.

[18] KIMURA T, NAKAMOTO T, OZAKI T, MIKI T. Microstructures and mechanical properties of aluminum-transition metal binary alloys (Al−Fe, Al−Mn, and Al−Cr) processed by laser powder bed fusion [J]. Journal of Alloys and Compounds, 2021, 872: 159571.

[19] QIU Yi, LI Ying-ju, FENG Xiao-hui, ZHANG Ang, YANG Yuan-sheng. Numerical simulation of microstructure evolution in molten pool of nickel-based superalloy during selective laser melting [J]. Transactions of Nonferrous Metals Society of China, 2024, 34: 560−575.

[20] SU Jin-long, JIANG Fu-lin, TENG Jie, CHEN Le-qun, YAN Ming, REQUENA G, ZHANG Lai-Chang, WANG Y M, OKULOV I V, ZHU Hong-mei. Recent innovations in laser additive manufacturing of titanium alloys [J]. International Journal of Extreme Manufacturing, 2024, 6: 032001.

[21] SHYAM A, PLOTKOWSKI A, BAHL S, SISCO K, ALLARD L F, YANG Y, HAYNES J A, DEHOFF R R. An additively manufactured AlCuMnZr alloy: Microstructure and tensile mechanical properties [J]. Materialia, 2020, 12: 100758.

[22] WANG Yue-ting, LI Rui-di, YUAN Tie-chui, ZOU Liang, WANG Min-bo, YANG Hai-ou. Microstructure and mechanical properties of Al−Fe−Sc−Zr alloy additively manufactured by selective laser melting [J]. Materials Characterization, 2021, 180: 111397.

[23] WANG Wen-yuan, TAKATA N, SUZUKI A, KOBASHI M, KATO M. Processability and optimization of laser parameters for densification of hypereutectic Al−Fe binary alloy manufactured by laser powder bed fusion [J]. Crystals, 2021, 11: 320.

[24] WANG Wen-yuan, TAKATA N, SUZUKI A, KOBASHI M, KATO M. Microstructural variations in laser powder bed fused Al−15%Fe alloy at intermediate temperatures [J]. Materials, 2022, 15(13): 4497.

[25] WEN Tao, LI Zhi-cheng, WANG Jian-ying, YANG Fei-peng, ZHU Meng-zhen, LUO Yi-mou, ZHANG Li-jun, LIU Zhi-lin, QIU Dong, YANG Hai-lin, JI Shou-xun. CALPHAD aided design of a crack-free Al−Mg−Si−Ti alloy with high strength: Heterogeneous nucleation and eutectic filling during additive manufacturing [J]. Virtual and Physical Prototyping, 2024, 19(1): e2378930.

[26] DUCHAUSSOY A, SAUVAGE X, EDALATI K, HORITA Z J, RENOU G, DESCHAMPS A, GEUSER F D. Structure and mechanical behavior of ultrafine-grained aluminum−iron alloy stabilized by nanoscaled intermetallic particles [J]. Acta Materialia, 2019, 167: 89−102.

[27] DORIN T, STANFORD N, BIRBILIS N, GUPTA R K. Influence of cooling rate on the microstructure and corrosion behavior of Al−Fe alloys [J]. Corrosion Science, 2015, 100: 396−403.

[28] NAYAK S S, CHANG H J, KIM D H, PABI S K, MURTY B S. Formation of metastable phases and nanocomposite structures in rapidly solidified Al−Fe alloys [J]. Materials Science and Engineering A, 2011, 528(18): 5967−5973.

[29] SHI Qian-yu, CHEN Ji-bing, CHEN Jun-sheng, WANG Yue-ting, XIA Xi-zhen, LI Rui-di. Additively manufactured fine-grained Al−Fe−Cu−Sc−Zr alloy with resistance to brittleness under high temperature [J]. Journal of Materials Research and Technology, 2024, 33: 7310−7324.

[30] XING Qi, TAKATA N, SUZUKI A, KOBASHI M, KATO M. Laser powder bed fusion of a near-eutectic Al−Fe binary alloy: Processing and microstructure [J]. Additive Manufacturing, 2020, 35: 101308.

[31] MISHRA R S, THAPLIYAL S. Design approaches for printability-performance synergy in Al alloys for laser-powder bed additive manufacturing [J]. Materials & Design, 2021, 204: 109640.

[32] KOU S. A criterion for cracking during solidification [J]. Acta Materialia, 2015, 88: 366−374.

[33] SAMES W J, LIST F A, PANNALA S, DEHOFF R R, BABU S S. The metallurgy and processing science of metal additive manufacturing [J]. International Materials Reviews, 2016, 61(5): 315−360.

[34] SIDAMBE A T, TIAN Y, PRANGNELL P B, FOX P. Effect of processing parameters on the densification, microstructure and crystallographic texture during the laser powder bed fusion of pure tungsten [J]. International Journal of Refractory Metals and Hard Materials, 2019, 78: 254−263.

[35] GU Dong-dong, HAGEDORN Y C, MEINERS W, MENG Guang-bin, BATISTA R J S, WISSENBACH K, POPRAWE R. Densification behavior, microstructure evolution, and wear performance of selective laser melting processed commercially pure titanium [J]. Acta Materialia, 2012, 60: 3849−3860.

[36] READ N, WANG Wei, ESSA K, ATTALLAH M M. Selective laser melting of AlSi10Mg alloy: Process optimisation and mechanical properties development [J]. Materials & Design, 2015, 65: 417−424.

[37] KIMURA T, NAKAMOTO T. Microstructures and mechanical properties of A356 (AlSi7Mg0.3) aluminum alloy fabricated by selective laser melting [J]. Materials & Design, 2016, 89: 1294−1301.

[38] GENG Hai-bin, LUO Jian, LI Jing-long, GAO Jian-jun, LIN Xin. Thermal boundary evolution of molten pool during wire

and arc additive manufacturing of single walls of 5A06 aluminum alloy [J]. Metals, 2020, 10(7): 848.

[39] RAGHAVAN N, DEHOFF R, PANNALA S, SIMUNOVIC S, KIRKA M, TURNER J, CARLSON N, BABU S S. Numerical modeling of heat-transfer and the influence of process parameters on tailoring the grain morphology of IN718 in electron beam additive manufacturing [J]. Acta Materialia, 2016, 112: 303−314.

[40] WU Yi-you, ZHANG Tao-mei, CHEN Chao, HOSSEINI S R E, ZHANG Xiao-yong, ZHOU Ke-chao. Microstructure and mechanical property evolution of additive manufactured eutectic Al−2Fe alloy during solidification and aging [J]. Journal of Alloys and Compounds, 2022, 897: 163243.

[41] QI Xing, TAKATA N, SUZUKI A, KOBASHI M, KATO M. Change in microstructural characteristics of laser powder bed fused Al−Fe binary alloy at elevated temperature [J]. Journal of Materials Science & Technology, 2022, 97: 38−53.

[42] PLOTKOWSKI A, SISCO K, BAHL S, SHYAM A, YANG Y, ALLARD L, NANDWANA P, ROSSY A M, DEHOFF R R. Microstructure and properties of a high temperature Al−Ce−Mn alloy produced by additive manufacturing [J]. Acta Materialia, 2020, 196: 595−608.

[43] UZAN N E, SHNECK R, YEHESKEL O, FRAGE N. High-temperature mechanical properties of AlSi10Mg specimens fabricated by additive manufacturing using selective laser melting technologies (AM-SLM) [J]. Additive Manufacturing, 2018, 24: 257−263.

[44] BI Jiang, LEI Zheng-long, CHEN Yan-bin, CHEN Xi, TIAN Ze, LU Nan-nan, QIN Xi-kun, LIANG Jing-wei. Microstructure, tensile properties and thermal stability of AlMgSiScZr alloy printed by laser powder bed fusion [J]. Journal of Materials Science & Technology, 2021, 69: 200−211.

[45] JIA Qing-bo, ZHUO Yu-hao, YAN Yu-qing, LU Cheng-qi, CHEN Zhen-yu, CHENG Yu-ang, WANG Chuan-yang. Tensile creep mechanisms of Al−Mn−Sc alloy fabricated by additive manufacturing [J]. Additive Manufacturing, 2024, 79: 103910.

[46] HU Mao-hui, ZHI Sheng-xing, CHEN Ji-bing, LI Rui-di, LIU Bo-wen, HE Liang, YANG Hui-hui, WANG Hong-ze. Restraint of intermetallic compound and improvement of mechanical performance of Ti/Al dissimilar alloy by rotary friction welding based on laser powder bed fusion [J]. Journal of Manufacturing Processes, 2024, 131: 440−454.

激光粉末床熔化制备耐热 Al−Fe−Mn 合金的显微组织和高温性能

陈俊升[1]，陈继兵[1]，石倩玉[1]，王悦婷[2]，夏熙珍[2]，李瑞迪[2]

1. 武汉轻工大学 机械工程学院，武汉 420023；
2. 中南大学 粉末冶金国家重点实验室，长沙 410083

摘 要：结合铸态合金激光重熔和非平衡液相投影热力学计算，设计了一种高强度、耐热的 Al−3Fe−2Mn 合金。将 Mn 原子加入到亚稳的纳米 Al_6Fe 相中，占据部分晶格位，提高了 Al_6Fe 相的热稳定性。另外，在激光粉末床熔合(L-PBF)快速凝固过程中，Fe 和 Mn 元素在铝合金中的溶解度显著提高，形成过饱和固溶体且强度提高。该合金具有优异的加工性能，相对密度超过 99%，200 ℃和 300 ℃的抗拉强度分别为 295 MPa 和 230 MPa。Al−3Fe−2Mn 合金具有较高的高温强度，具有广阔的应用前景。

关键词：Al−Fe−Mn 合金；激光粉末床熔化；高温强度；显微组织；耐热性

(Edited by Bing YANG)